Interference Dips in the Single-Crystal Absorption Spectrum of the Tri-μ-fluoro−Bis(trifluorochromate(III)) Complex

Ralph Schenker,[†] Myriam Triest,[‡] Christian Reber,*[,‡] and Hans U. Güdel*[,†]

Departement für Chemie, Universität Bern, CH-3000 Bern 9, Switzerland, and Département de chimie, Université de Montréal, Montréal QC H3C 3J7, Canada

Received December 6, 2000

The lowest energy spin-allowed crystal field band of $(Et_4N)_3Cr_2F_9$ shows a distinct interference dip at 15000 cm^{-1} with an approximate width of 200 cm^{-1}. This spectroscopic feature is due to spin−orbit coupling between the ^2E and $^4T_2$ excited states and is analyzed with a set of two coupled potential energy surfaces. The minimum of the $^4T_2$ potential surface is displaced along at least two normal coordinates. The modes involved cannot be directly determined from the unresolved absorption spectrum, but are obtained from Raman spectra and from the well-resolved spin-forbidden crystal field transition to the $^2A_1$ state. The first mode with a frequency of 415 cm^{-1} has predominant Cr−F stretching character; the second mode has a frequency of 90 cm^{-1} and involves the entire $Cr_2F_9^{3-}$ dimer.

Introduction

Electronic transitions involving interacting states often lead to unusual band shapes in electronic spectra. Interference effects between the states can be constructive, as illustrated by the intensity borrowing of forbidden transitions well separated from allowed bands, or destructive, as illustrated in the following for interference dips near the band maximum of a broad allowed transition. Antiresonances were described and theoretically analyzed for atomic spectra by Fano[1,2] and are often called "Fano antiresonances" even in molecular and solid state spectra, where one of the crucial prerequisites of the original theory by Fano, namely, a very slowly varying intensity of the allowed transition over a wide frequency range, is no longer fulfilled. The majority of interference dips in transition metal compounds have been observed in the absorption spectra of chromophores with the d^3 electron configuration, such as solids containing Cr^{3+} and V^{2+} ions.[3−7] These studies were often made on chromium(III)-doped glasses or host lattices, where the site of the chromophore is ill-defined and the interference dip can be significantly affected by inhomogeneous broadening. A key condition for the observation of interference dips is a narrow, forbidden transition with an energy close to the maximum of a broad, allowed band. This situation can occur for complexes with one or several metal centers. The detailed molecular structure has to be considered for an analysis of such spectra, because even small structural variations can change excited state energies by hundreds of wavenumbers, often sufficient to prevent distinct interference dips. Spectra are usually analyzed with Fano's equations,[1,2] which are fitted to the spectrum after a suitable, often somewhat arbitrary, background function is subtracted from the experimental data. This procedure is easily performed, but is not physically meaningful, as was recently demonstrated from a rigorous theoretical perspective.[8]

The 10 K polarized absorption spectra of the tri-μ-fluoro bridged Cr^{3+} dimer in $(Et_4N)_3Cr_2F_9$ show several clear interference dips. A detailed analysis of all ligand field transitions and of the exchange interactions in this dimer is given elsewhere.[9] The chromophores are well-characterized by single-crystal X-ray diffraction.[10] We present and apply a molecular model based on coupled potential energy surfaces for two excited states. This allows us to reproduce the lowest energy ligand field band with its interference dip in $(Et_4N)_3Cr_2F_9$, without subtraction of a background from the experimental spectrum. Both the vibrational and electronic spectra are used to characterize the interference dip. The surfaces are defined using transition energies from the absorption spectrum and vibrational energies from the Raman spectrum, leaving only very few parameters that have to be adjusted in order to obtain a calculated spectrum in good agreement with the experiment. This approach has been shown to lead to absorption band shapes with interference dips.[11] It has also been used to analyze coupled excited states in $Ni(H_2O)_6^{2+}$,[12] where one-dimensional potentials defined along the totally symmetric stretching mode of an octahedral complex are sufficient to quantitatively rationalize spectra with resolved vibronic structure influenced by the coupled electronic states. In the following, we apply this approach to the title complex and show how to define a model involving multiple normal coordinates, even if the absorption spectrum does not show resolved vibronic structure.

[†] Universität Bern.

[‡] Université de Montréal.

(1) Fano, U. *Phys. Rev.* **1961**, *124*, 1866.

(2) Fano, U.; Cooper, J. W. *Phys. Rev. A* **1965**, *137*, 1364.

(3) Sturge, M. D.; Guggenheim, H. J.; Pryce, M. H. L. *Phys. Rev. B* **1970**, *2*, 2459.

(4) Bermudez, V. R.; McClure, D. S. *J. Phys. Chem. Solids* **1979**, *40*, 129.

(5) Lempicki, A.; Andrews, L.; Nettel, S. J.; McCollum, B. C.; Solomon, E. I. *Phys. Rev. Lett.* **1980**, *44*, 1234.

(6) Voda, M.; Garcia-Solé, J.; Vergara, I.; Kaminskii, A.; Mill, B.; Butashin, A. *Phys. Rev. B* **1994**, *49*, 3755.

(7) Rodrìguez-Mendoza, U. R.; Rodrìguez, V. D.; Lavin, V.; Martin, I. R.; Nuñez, P. *Spectrochim. Acta* **1999**, *A55*, 1319.

(8) Neuhauser, D.; Park, T.-J.; Zink, J. I. *Phys. Rev. Lett.* **2000**, *85*, 5304.

(9) Schenker, R.; Heer, S.; Güdel, H. U.; Weihe, H. *Inorg. Chem.* **2001**, *40*, 1482.

(10) Krämer, K. W.; Schenker, R.; Hauser, J.; Weihe, H.; Güdel, H. U.; Bürgi, H.-B. *Z. Anorg. Allg. Chem.* **2001**, *627*, 2511.

(11) Reber, C.; Zink, J. I. *J. Chem. Phys.* **1992**, *96*, 2681.

(12) Bussière, G.; Reber, C. *J. Am. Chem. Soc.* **1998**, *120*, 6306.

10.1021/ic001364v CCC: $20.00

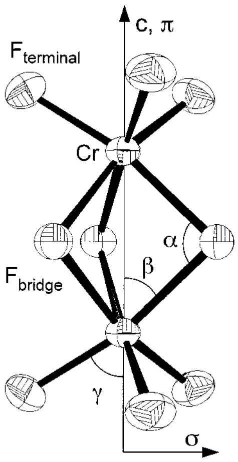

Figure 1. Molecular structure, polarization directions, and crystallographic *c* axis for the title complex.

Table 1. Selected Interatomic Distances (Å) and Angles (deg) in the $[Cr_2F_9]^{3-}$ Dimer[a]

Cr•••Cr	2.769
$Cr-F_{bridge}$	1.994
$Cr-F_{terminal}$	1.854
$Cr-F_{bridge}-Cr$ (α)	87.94
β	46.03
γ	58.20

[a] The labeling refers to Figure 1.

Experimental Section

The synthesis of the title complex is described elsewhere in detail.[9] Crystals of $(Et_4N)_3Cr_2F_9$ were obtained as brown needles from DMF solutions upon slow cooling from 130 °C to room temperature within 48 h. The product is very hygroscopic and decomposes completely within minutes when exposed to air; all crystals were thus stored and handled under nitrogen in a drybox. The compound crystallizes in the hexagonal space group $P6_3/m$ (No. 176) with the trigonal dimer axis parallel to the *c* axis, the hexagonal axis of the crystal.[10] The full crystal structure is reported elsewhere.[10] Figure 1 shows an ORTEP plot of the $Cr_2F_9^{3-}$ dimer, and the relevant angles and interatomic distances are listed in Table 1.

Polarized single-crystal absorption spectra were measured between 770 and 385 nm in both *π* and *σ* polarization, i.e., with the electric dipole vector of the light parallel and perpendicular to the *c* axis, respectively, as defined in Figure 1. Spectra are shown for a single crystal with a thickness of 105 μm and a surface of 370 × 150 μm^2 containing the *c* axis. The absorbance of our $(Et_4N)_3Cr_2F_9$ crystal was too high to measure the intense $^4T_1(^4F)$ band between 18000 and 25000 cm^{-1} in *π* polarization. We measured this band using a $(Et_4N)_3Fe_2F_9$ crystal doped with 6% Cr^{3+}, since the host lattice is transparent below 25000 cm^{-1}. The intensity of the resulting spectrum was scaled to that of pure $(Et_4N)_3Cr_2F_9$ using the $^4T_2$ band. Thus, in the spectra shown in Figure 2a, only the $^4T_1(^4F)$ band between 18000 and 25000 cm^{-1} in *π* polarization originates from the doped $(Et_4N)_3Fe_2F_9:Cr^{3+}$ sample. Absorption spectra were recorded on a Cary 5E double-beam spectrometer with the sample cooled to 10 K in a closed-cycle helium refrigerator (Air Products). Raman spectra were measured on polycrystalline samples at 80 K with a Renishaw System 3000 spectrometer using the 514.5 nm line of an Ar^+ ion laser as the excitation source.

Calculations of normal mode frequencies were carried out with the Gaussian software package,[13] using the Kohn−Sham density functional method in conjunction with the PBE hybrid approximation[14−16] for the exchange-correlation energy. The atomic coordinates from the crystal structure determination were used as a starting point for the geometry optimization, and the basis set keyword employed was LANL2DZ. The full output of the calculation is given as Supporting Information.

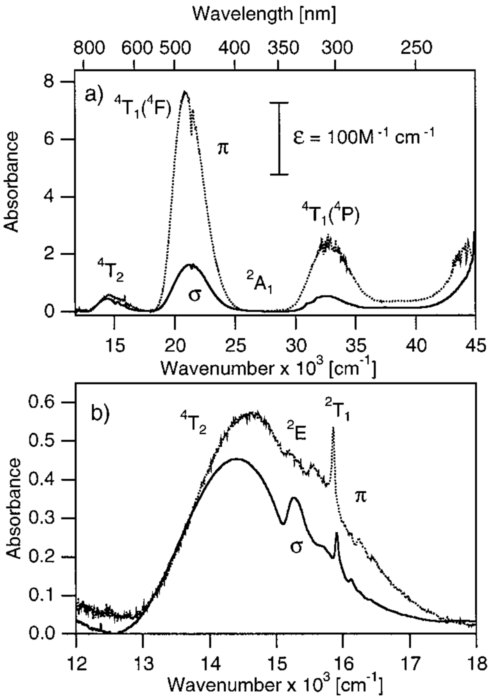

Figure 2. *σ* (solid lines) and *π* (dotted lines) polarized spectra of $(Et_4N)_3Cr_2F_9$ at 10 K. The bands are labeled in *O* notation.

Spectroscopic Results

Figure 2a shows *σ* (solid line) and *π* (dotted line) polarized 10 K absorption spectra of $(Et_4N)_3Cr_2F_9$ in the visible spectral region. These overall spectra show the usual three spin-allowed bands expected for octahedral chromium(III) complexes, and we use *O* point group labels for simplicity throughout the following, neglecting the lower symmetry trigonal crystal field at the chromium(III) sites. The spectrum in the region of the lowest energy spin-allowed band is shown in detail in Figure 2b for a pure $(Et_4N)_3Cr_2F_9$ single crystal. The features built on the high-energy side of the broad, unresolved $^4T_2$ band above 14500 cm^{-1} are due to the $^4A_2 \rightarrow {}^2E$, $^2T_1$ transitions. We observe a distinct antiresonance dip at 15000 cm^{-1}, which is more pronounced in *σ* polarization. The interference dip in this *σ* polarized spectrum will be discussed in detail in the following. Its width is on the order of 200 cm^{-1}, larger by at least an order of magnitude than the sharp resolved peaks at higher energy. This comparison indicates that the interference dip is not dominated by inhomogeneous broadening. Above 15800 cm^{-1}, a number of sharp absorption bands are superimposed on the

---

(13) Frisch, M. J.; Trucks, G. W.; Schlegel, H. B.; Scuseria, G. E.; Robb, M. A.; Cheeseman, J. R.; Zakrzewski, V. G.; Montgomery, J. A., Jr.; Stratmann, R. E.; Burant, J. C.; Dapprich, S.; Millam, J. M.; Daniels, A. D.; Kudin, K. N.; Strain, M. C.; Farkas, O.; Tomasi, J.; Barone, V.; Mennucci, B.; Cossi, M.; Adamo, C.; Jaramillo, J.; Cammi, R.; Pomelli, C.; Ochterski, J.; Petersson, G. A.; Ayala, P. Y.; Morokuma, K.; Malick, D. K.; Rabuck, A. D.; Raghavachari, K.; Foresman, J. B.; Ortiz, J. V.; Cui, Q.; Baboul, A. G.; Clifford, S.; Cioslowski, J.; Stefanov, B. B.; Liu, G.; Liashenko, A.; Piskorz, P.; Komaromi, I.; Gomperts, R.; Martin, R. L.; Fox, D. J.; Keith, T.; Al-Laham, M. A.; Peng, C. Y.; Nanayakkara, A.; Challacombe, M.; Gill, P. M. W.; Johnson, B.; Chen, W.; Wong, M. W.; Andres, J. L.; Gonzalez, C.; Head-Gordon, M.; Replogle, E. S.; Pople, J. A. *Gaussian 01*, development version (revision A.01-) ed.; Gaussian, Inc.: Pittsburgh, PA, 2001.

(14) Perdew, J. P.; Burke, K.; Ernzerhof, M. *Phys. Rev. Lett.* **1996**, *77*, 3865.

(15) Perdew, J. P.; Ernzerhof, M.; Burke, K. *J. Chem. Phys.* **1996**, *105*, 9982.

(16) Ernzerhof, M.; Scuseria, G. E. *J. Chem. Phys.* **1999**, *110*, 5029.

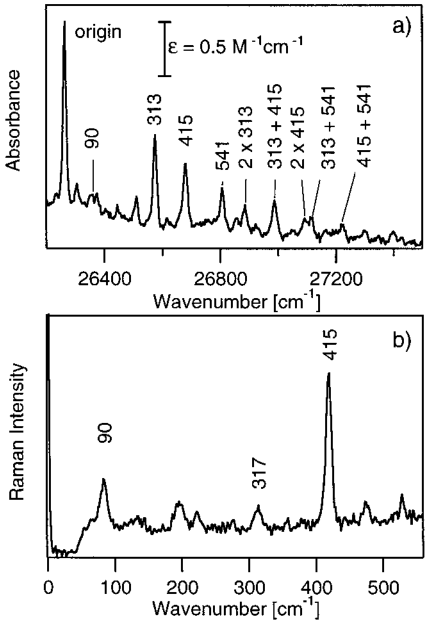

Figure 3. (a) π polarized 11 K absorption spectrum of the $^4A_2 \rightarrow {}^2A_1$ one-electron excitation. The prominent vibrational sideband lines are indicated with their energy separation from the electronic origin. (b) Unpolarized 80 K Raman spectrum.

$^4T_2$ band. We assign the dip at 15000 cm^{-1} and the sharp bands above 15800 cm^{-1} to $^4A_2 \rightarrow {}^2E$ and $^4A_2 \rightarrow {}^2T_1$ transitions, respectively, in analogy to related chloride complexes. [9,17] Near the maximum of the $^4T_1(^4F)$ band, three additional antiresonance dips at 21415, 21695, and 21970 cm^{-1} are observed in both polarizations, with energy separations of 280 cm^{-1} between minima. They are due to the $^4A_2 \rightarrow {}^2T_2$ transitions. Their positions as well as their depths relative to the intensity of the broad $^4T_1$ band are identical in both polarizations.

Ingredients essential to our analysis of the interference dips are the Cr−F vibrational frequencies. None of the intense bands in Figure 2 show any resolved vibronic structure. However, the 11 K absorption spectrum of the $^4A_2 \rightarrow {}^2A_1$ one-electron excitation at 11 K obtained from a pure $(Et_4N)_3Cr_2F_9$ crystal shows well-resolved vibronic structure based on a prominent origin at 26263 cm^{-1}, shown in Figure 3a. Several progressions in three molecular modes with frequencies of 313, 415, and 541 cm^{-1} are indicated. These modes have to be totally symmetric because both the initial and final states of the electronic transition are nondegenerate. The excited state frequencies are expected to be close to the corresponding ground state modes because the progressions are short, allowing us to compare absorption and Raman spectra. The absorption spectrum thus allows us to identify all relevant modes to define our model for the interference dip. The well-resolved absorption spectrum in Figure 3a is compared to the unpolarized 80 K Raman spectrum in Figure 3b, illustrating the correspondence of vibrational frequencies. The Raman spectrum also contains vibrational transitions which correspond to modes localized on the $(Et_4N)^+$ counterion. It is important to note that the two most intense signals at 90 and 415 cm^{-1} correspond to frequencies also observed in the absorption spectrum in Figure 3a. These modes are therefore clearly identified as modes of the title complex in Figure 1 and will be used throughout the following discussion. Table 2 summarizes these experimental vibrational frequencies.

Table 2. Experimental and Calculated Vibrational Frequencies of Selected Totally Symmetric Modes Obtained from Raman and Absorption Spectra and from Density Functional Calculations Using the Crystallographic Structure in Figure 1

assignment[a]	Raman (cm^{-1})	absorption[b] (cm^{-1})	calcd for $Cr_2F_9^{3-}$ (cm^{-1})
low-frequency vibronically active modes	90	90	94 (a, C_3) 108 (e′, C_{3h}, D_{3h}) 176 (a$_1$′, a′, C_{3h}, D_{3h})
$CrF_{bridge}Cr$, $Cr-F_{terminal}$	317, 415	313, 415	320, 447
$Cr-F_{terminal}$	533	541	597

[a] From calculated normal coordinates. [b] From the $^4A_2 \rightarrow {}^2A_1$ absorption band in Figure 3.

Discussion

Molecular Structure, Electronic States, and Normal Modes. The molecular structure of the title complex is shown in Figure 1. The single ion and dimer point group symmetries are C_3 and C_{3h}, respectively. The deviation from the ideal D_{3h} symmetry is small and arises from a rotation of the $(F_{bridge})_3$ plane around the C_3 axis by 2.3°, destroying the vertical symmetry planes. Figure 1 clearly shows the trigonal distortion from perfect octahedral symmetry at the site occupied by the chromium(III) ion. Each chromium(III) center has bonds to three terminal and to three bridging fluoride ligands. The angle γ between the trigonal axis and the $Cr-F_{terminal}$ bond is increased from 54.74° to 58.20°, corresponding to a trigonal compression. The $Cr-F_{terminal}$ bond length is 1.854 Å**.** In contrast, the $Cr(F_{bridge})_3Cr$ core is elongated along the trigonal axis, with an angle β of 46.03° between $Cr-F_{bridge}$ bonds and the trigonal axis and a $Cr-F_{bridge}$ bond length of 1.994 Å (see Table 1). The total trigonal crystal field created by terminal and bridging ligands is expected to be small, as the two different distortions partially cancel. The band maxima and widths of the spin-allowed bands in the spectra of Figure 2 confirm the small trigonal splitting,[9] justifying our use of O symmetry labels for electronic states. Spin-forbidden bands are resolved and observed as narrow peaks or interference dips, illustrated in Figure 2b. Their number is higher than expected for a CrF_6^{3-} complex with perfect octahedral symmetry, and they correspond to transitions to both the ^2E and $^2T_1$ states. Spinor components of doublet states with the same symmetry as a nearby quartet component can give rise to interference dips if the two states have a sufficiently large coupling constant. Transitions to doublet states with symmetries different from any nearby quartet component are observed as sharp peaks, which can be either electronic origins or vibronic origins of the ^2E and $^2T_1$ states split by spin−orbit coupling, by the trigonal crystal field, and by exchange interaction. The observed set of peaks and interference dips is too complicated for a straightforward assignment to individual electronic and vibronic transitions in the actual point group of the title complex.

In order to characterize the normal coordinates in the dimer, we use calculated frequencies obtained from the density functional analysis of the title complex.[13] We have calculated all molecular vibrational frequencies for the full $Cr_2F_9^{3-}$ complex in the optimized geometry resulting from the calculation. This structure deviates slightly from D_{3h} idealized symmetry, but this deviation is within the convergence criteria used and leads to splits of less than 2 cm^{-1} between components of modes that are degenerate in D_{3h} point group symmetry. The model for these calculations was limited to a single anion, and no cations or positive charges were defined to compensate the total charge. The most important frequencies of modes that can lead to progressions in the absorption spectra and a qualitative

---

(17) Briat, B.; Russel, M. F.; Rivoal, J. C.; Chapelle, J. P.; Kahn, O. *Mol. Phys.* **1977**, *34*, 1357.

description of their normal coordinates are given in Table 2. The binuclear complex has low-frequency molecular modes below 180 cm^{-1} which are absent in a complex with only one chromium(III) center, but an otherwise identical ligand sphere. These low-frequency modes involve bending or tilting of the six $F_{terminal}$ ligands with respect to the $Cr(F_{bridge})_3Cr$ fragment. The lowest frequency mode is calculated at 94 cm^{-1} and transforms totally symmetric in the C_3 point group of the single ion. The lowest frequency totally symmetric mode in idealized D_{3h} symmetry is calculated at 176 cm^{-1}, and the Raman active e′ mode, which can also form progressions in bands involving the degenerate $^4T_2$ state, has a calculated frequency of 108 cm^{-1}. The population of the σ antibonding e orbitals upon the $^4A_2 \rightarrow {}^4T_2$ excitation is likely to involve such low-frequency modes, because the $Cr-F_{bridge}$ bonds cannot stretch without deformation of the $Cr-F_{bridge}-Cr$ angle in the title dimer, an important consequence of the structure in Figure 1. The calculated frequencies are in satisfactory agreement with experimental results. The assignments in Table 2 are further supported by the experimental frequency of the totally symmetric mode of exactly octahedral CrF_6^{3-} molecular units obtained by doping Cr^{3+} into K_2NaGaF_6. It is observed at 568 cm^{-1},[18] similar to our experimental values of 533 and 541 cm^{-1} obtained from the Raman and absorption spectra in Figure 3, respectively, and to the calculated value of 597 cm^{-1} listed in Table 2. We calculate the $F_{terminal}CrF_{bridge}CrF_{terminal}$ stretching modes of the title complex at 320 cm^{-1}, very close to the experimental frequencies of 317 and 313 cm^{-1}. A detailed normal coordinate analysis of the higher symmetry (D_{3h}) $Cr_2Cl_9^{3-}$complex in $K_3Cr_2Cl_9$ identifies a corresponding frequency as 299 cm^{-1},[19] which is lower in energy than in the title complex and thus qualitatively confirms our assignment. At 447 cm^{-1}, we calculate a mode with predominant $CrF_{bridge}Cr$ stretching character, very close in energy to the prominent peaks at 415 cm^{-1} in the Raman and absorption spectra of Figure 3. This comparison of experimental and calculated vibrational frequencies allows us to identify the normal modes for our calculation of the interference dip in the absorption spectrum.

Potential Energy Surfaces of the Coupled Electronic States. The model used in the following consists of a single quartet ($^4T_2$) and a single doublet (^2E) excited state with potential energy surfaces used to calculate absorption spectra and to characterize the interference dip observed at 15000 cm^{-1} in Figure 2b. The trigonal, spin−orbit, and exchange splittings as well as all other doublet and quartet excited states are neglected. Spin−orbit coupling between the two states is the physical origin for the antiresonance. The two excited states are represented by harmonic potentials along one or two normal coordinates. We examine one-dimensional potential surfaces along two different normal coordinates. For our first model, we use the normal coordinate corresponding to the totally symmetric Cr−F stretching mode observed at 415 cm^{-1}, a value that also represents an average of the stretching frequencies involving both the terminal and bridging fluoride ligands, observed at frequencies between 400 and 560 cm^{-1} in the title compound and related complexes. For the second calculation, we use a value of 90 cm^{-1}, the lowest observed frequency of the $Cr_2F_9^{3-}$. In our model, this mode represents the lowest frequency totally symmetric mode of the single-ion or dimer point groups and the e′ mode of the dimer in C_{3h} or idealized D_{3h} point group symmetry. Their exact frequencies in the $^4T_2$ and ^2E excited states are not known from experiments, but the density functional calculation for the electronic ground state provides reasonable upper limits. This choice illustrates the effects of modes with frequencies below 200 cm^{-1} on the absorption spectrum. Finally, we combine the two modes and use two-dimensional potential energy surfaces to obtain the best agreement with the experimental spectrum, indicating that several modes in the wavenumber ranges given above are contributing to the observed band shape with the narrow interference dip.

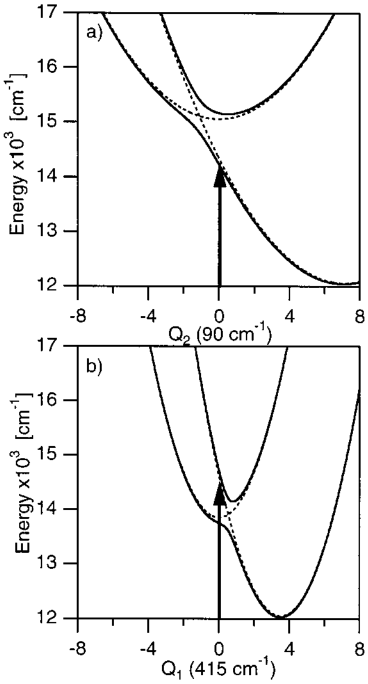

Figure 4. Potential energy curves for the $^4T_2$ and ^2E excited states. Diabatic (harmonic) and adiabatic (coupled) potentials are shown as dotted and solid lines, respectively. The origin of the Q_i axis corresponds to the ground state equilibrium geometry. These potentials are used to calculate the spectra in Figure 6a,b. The arrow denotes the Franck−Condon absorption transition. (a) Vibrational frequency 90 cm^{-1}. (b) Vibrational frequency 415 cm^{-1}.

In the first two models, each harmonic potential is defined along a single normal coordinate (Q_i) with its frequency k_i in wavenumber units. The index i represents either the 90 cm^{-1} mode or the 415 cm^{-1} mode. The position of the potential minimum and the vibrational frequency for the ^2E state are identical to the ground state potential minimum, set to $Q_i = 0$. The position of the $^4T_2$ minimum is shifted to higher values of Q_i by an amount ΔQ_i, a parameter determined from the calculated spectra, and we again assume its vibrational frequencies to be identical to those of the ground and doublet excited states. All normal coordinates Q_i used in the following are in dimensionless units.

The potentials for the two excited states in the absence of spin−orbit coupling are given by

$$V(^2E) = \frac{1}{2}\sum_i (k_i Q_i^2) + E(^2E) \qquad (1)$$

$$V(^4T_2) = \frac{1}{2}\sum_i (k_i (Q_i - \Delta Q_i)^2) + E(^4T_2) \qquad (2)$$

These potentials are shown as dotted lines in Figure 4 along both normal coordinates discussed here. The crossing of the

---

(18) Ferguson, J.; Guggenheim, H. J.; Wood, D. L. *J. Chem. Phys.* **1971**, *54*, 504.

(19) Black, J. D.; Dunsmuir, J. T. R.; Forrest, I. W.; Lane, A. P. *Inorg. Chem.* **1975**, *14*, 1257.

potentials occurs at Q values close to the ground state potential minimum, indicated by the vertical arrows in Figure 4. This is an important prerequisite for prominent interference dips.[11] For all calculations in the following, we consider the transition to the diabatic $^4T_2$ state defined by eq 2 to be fully allowed and the transition to the ^2E state described by eq 1 to be completely forbidden. We do not attempt to include the polarization of the experimental spectrum in our model. All intensity observed for the doublet band is therefore borrowed from the transition to the quartet state.

The $^4T_2$ and ^2E excited state potentials are coupled by a constant, off-diagonal matrix element V_{12}. Its magnitude is on the order of the spin−orbit coupling constant ζ. The coupled ^2E and $^4T_2$ potentials are defined by

$$V(^2\mathrm{E},{}^4\mathrm{T}_2) = \begin{pmatrix} \frac{1}{2}\sum_i (k_i Q_i^2) + E(^2E) & V_{12} \\ V_{12} & \frac{1}{2}\sum_i (k_i (Q_i - \Delta Q_i)^2) + E(^4T_2) \end{pmatrix} \quad (3)$$

The adiabatic potentials shown as solid lines in Figure 4 correspond to the eigenvalues of the matrix in eq 3. Their doublet and quartet character varies along each normal coordinate Q_i and can be obtained from the eigenvectors of eq 3.

This model is easily extended to two (or more) normal coordinates by allowing the index i in eqs 1−3 to have two (or more) values. We denote the normal coordinate of the 415 and 90 cm^{-1} modes as Q_1 and Q_2, respectively, throughout the following**.** Both two-dimensional adiabatic potentials are shown in a perspective view in the top part of Figure 5. The corresponding upper and lower adiabatic potentials are shown as contour plots in the middle and bottom panels of Figure 5, respectively. It is obvious that the band maximum of the allowed transition will occur near the avoided crossing of the surfaces. Figure 5 illustrates that the complicated shape of the potentials is due to the different frequencies of the modes, to the offsets ΔQ_i of the $^4T_2$ state along both normal coordinates, and to the energy difference between the two potentials. All these parameters have to be defined in order to calculate a spectrum. This list of parameters illustrates that models involving more than two electronic states and normal modes become prohibitively difficult to reliably define from spectra as shown in Figure 2.

Absorption Spectra Calculated from the Model Potential Surfaces. In this section, we compare calculated band shapes of the $^4T_2/^2E$ band with the σ polarized experimental spectrum of the pure $(Et_4N)_3Cr_2F_9$ crystal in Figure 2b. We use time-dependent theory to calculate absorption spectra, as it provides a unified approach for all potentials in eqs 1−3 of the preceding section. Absorption spectra are calculated as[20,21]

$$I_{\mathrm{abs}}(\omega) = \omega \int_{-\infty}^{\infty} e^{i\omega t} \langle \phi | \phi(t) \rangle e^{-\Gamma^2 t^2}\, dt \quad (4)$$

The most important part of this equation is the autocorrelation function $\langle \phi | \phi(t) \rangle$. It depends strongly on the potential surfaces in the region explored by the time-dependent wave packet[22] and will allow us to examine the differences between one-dimensional and two-dimensional models. Γ is a phenomenological damping factor for all calculations in order to reproduce the resolution of the experimental spectra. Its numerical values are given in Table 3.

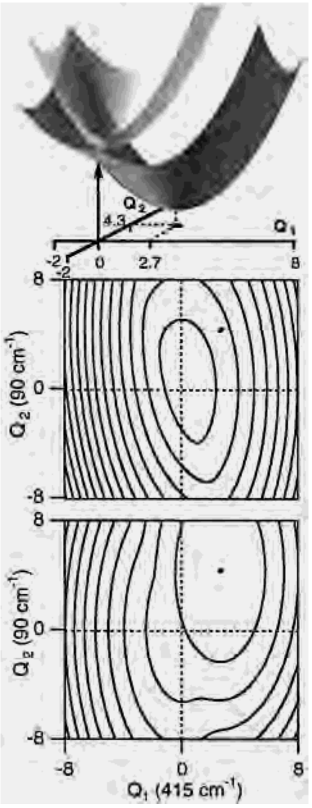

Figure 5. Coupled potential surfaces. Top: perspective view. Middle and bottom: upper and lower adiabatic potential energy surfaces obtained from the parameter values in Table 3 for the two-mode model. The origin of the (Q_1,Q_2) coordinate system denotes the ground state equilibrium geometry, and the dot in the contour plots and in the (Q_1,Q_2) plane of the perspective view indicates the minimum of the $^4T_2$ potential surfaces.

Table 3. Parameter Values Used for the Calculation of the Absorption Spectra in Figure 6[a]

	one-mode model		two-mode model,
parameter	Figure 6a	Figure 6b	Figure 6c
k_1 (cm^{-1})		415	415
k_2 (cm^{-1})	90		90
ΔQ_1		3.52	2.68
ΔQ_2	7.12		4.27
$E(^4T_2)$ (cm^{-1})	12050	12050	12050
$E(^2E)$ (cm^{-1})	15050	13850	14800
V_{12} (cm^{-1})	300	300	300
Γ (cm^{-1})	125	170	165

[a] Parameters are defined in eqs 1−3.

Spectra for one-dimensional potentials can be calculated with a split-operator method described in detail previously.[11,23] The time-dependent wave function for the two coupled states is defined by two arrays of n values on a closely spaced grid along the normal coordinate Q_i. A typical value for n used in our calculations is 1024. For potential surfaces defined along f normal coordinates, this method becomes inefficient as we need to keep track of n^f grid points defining the potential surfaces and the time-dependent wave functions at each time step. We have developed an alternative approach.[24] Instead of using an

---

(20) Heller, E. J. *Acc. Chem. Res.* **1981**, *14*, 368.

(21) Zink, J. I.; Kim Shin, K.-S. Molecular distortions in excited electronic states determined from electronic and resonance Raman spectroscopy. In *Advances in Photochemistry*; Volman, D. H., Hammond, G. S., Neckers, D. C., Eds.; John Wiley: New York, 1991; Vol. 16, p 119.

(22) Heller, E. J. *J. Chem. Phys.* **1975**, *62*, 1544−1555.

(23) Feit, M. D.; Fleck, J. A., Jr.; Steiger, A. *J. Comput. Phys.* **1982**, *47*, 412.

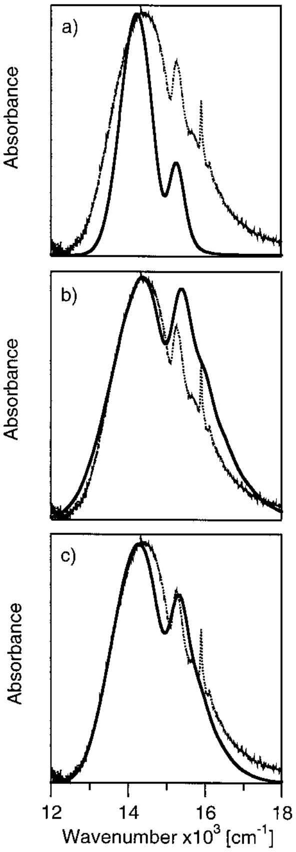

Figure 6. Comparison of experimental and calculated absorption spectra: (a) Calculation with one-dimensional potentials as shown in Figure 4a for the 90 cm^{-1} mode. (b) Calculation with one-dimensional potentials as shown in Figure 4b for the 415 cm^{-1} mode. (c) Calculated spectrum with the coupled two-dimensional potentials shown in Figure 5 with frequencies of 90 and 415 cm^{-1}.

f-dimensional grid to describe the time-dependent wave function in coordinate space, we use a Chebyshev expansion method introduced by Kosloff et al.[24−28] The wave function is defined by a one-dimensional set of coefficients for an optimized set of typically fewer than 30 basis functions, allowing for a much more efficient propagation.

Experimental and calculated spectra are compared in Figure 6. Panels a and b of Figure 6 show spectra calculated with one-dimensional potentials along the 90 and 415 cm^{-1} normal coordinates, respectively. These potentials are shown in Figure 4. With the low-frequency mode, we obtain a narrow interference dip, in agreement with the experiment, but with an overall calculated band shape that is much too narrow and a maximum on the high-energy side of the interference dip that is significantly too low, as shown in Figure 6a. The width of the spectrum necessitates a very large offset ΔQ along this coordinate, as all other offsets are zero. The value of 7.12 in Table 3 corresponds to a Huang−Rhys parameter S of 25, a very large value for this d−d transition. The single-coordinate model involving the low-frequency mode is therefore not physically meaningful, even though it reproduces the interference dip. The spectrum calculated with the 415 cm^{-1} mode in Figure 6b reproduces the onset of the band and the first maximum well, but the calculated antiresonance is too wide by approximately a factor of 5 and the high-energy part of the spectrum is not well described. The Huang−Rhys parameter for this model is S = 6.2, a value at the upper limit of the range determined for chromium(III) complexes with chloride and bromide ligands.[29] The large ΔQ_i and S values indicate that most likely more than one normal coordinate contributes to the observed band shape. These two calculated spectra show that interference dips can occur in bands that are completely characterized by a single-coordinate model, and they illustrate the correlation between overall bandwidths and the width of the interference dip. In the following, we rationalize the shape of the interference dip in Figure 2b with a model combining both the high- and low-frequency modes.

The model involving two-dimensional potential surfaces leads to a considerably better agreement between experimental and calculated spectra, as shown in Figure 6c. We note that the onset and first maximum of the band are reasonably reproduced, and the description of the interference dip and the maximum at its high-energy side is better than for the one-dimensional models. This two-mode model is physically reasonable, since it involves high-frequency Cr−F modes known to form progressions in the spectra of mononuclear complexes, and a low-frequency mode that only occurs in the dimer, observed both in the absorption and Raman spectra of Figure 3. The ΔQ_i values are smaller than for the one-mode models and correspond to Huang−Rhys parameters S of 3.6 and 9.1 for the 415 and 90 cm^{-1} modes, respectively. The large parameter for the low-frequency mode is specific to the $Cr_2F_9^{3-}$ dimer; it has been shown that the bandwidth of the corresponding transition in octahedral CrX_6^{3-} halide complexes is determined by high-frequency totally symmetric and Jahn−Teller active modes.[18,29] The comparison of the models illustrates that it is not possible to determine reliable ΔQ_i values from spectra without resolved vibronic structure. We therefore do not attempt to calculate molecular bond length changes for the $^4T_2$ state from the potential surfaces used to obtain the theoretical absorption spectra. Resonance Raman excitation profiles across the region of Figure 2b could in principle define each ΔQ_i, but the resonance enhancements for the weak d−d transitions in Figure 2b are excessively difficult to measure with the required precision.

Our two-mode model shows a significant improvement over the one-mode models, indicating that the $^4T_2$ state is displaced along several normal coordinates. The experimental spectrum does not allow us to determine the parameters needed for a model involving more than two modes. A more realistic model should also include the trigonal, spin−orbit, and exchange splittings of both the $^4T_2$ and ^2E states. However, our model based on only two electronic states and two molecular modes is the simplest choice that leads to a reasonable agreement between calculated and experimental spectra, and the two frequencies chosen can be viewed as effective values, representing an average of the potentially large number of modes with nonzero ΔQ_i values. This simple model illustrates the origin of the interference dip.

Autocorrelation Functions and Comparison of Models. The most important differences between the one- and two-mode models can be rationalized from the potential energy surfaces in Figure 5, which show the adiabatic potentials used for the calculations in Figure 6c. It is important to emphasize that our model calculations are not based on the adiabatic approximation,

---

(24) Cromp, B.; Triest, M.; Carrington Jr., T.; Reber, C. *Spectrochim. Acta A* **1999**, *55*, 575.
(25) Kosloff, R. *J. Phys. Chem.* **1988**, *92*, 2087.
(26) Tal-Ezer, H.; Kosloff, R. *J. Chem. Phys.* **1994**, *81*, 3967.
(27) Friesner, Z. R. A.; Wyatt, R. E.; Hempel, C.; Criner, B. *J. Comput. Phys.* **1986**, *64*, 220.
(28) Roy, P.-N.; Carrington, T. *Chem. Phys. Lett.* **1996**, *257*, 98.
(29) Knochenmuss, R. D.; Reber, C.; Rajasekharan, M. V.; Güdel, H. U. *J. Chem. Phys.* **1986**, *85*, 4280.

but *we use* the adiabatic surfaces in Figure 5 to illustrate the fundamental differences between one-mode and two-mode models. The two contour plots in Figure 5 show the upper and lower adiabatic potential surfaces, respectively. They are the two-dimensional analogues of the one-dimensional adiabatic potential surfaces in Figure 4, but no cross section along Q_1 or Q_2 in Figure 5 corresponds exactly to the potentials in Figure 4. The spin-allowed Franck–Condon transition occurs at the origin of the (Q_1,Q_2) coordinate system and ends on the diabatic surface of the $^4T_2$ state, as indicated by the arrows in Figure 4. In the one-mode model based on the high-frequency mode, corresponding to a cross section along $Q_2 = 0$, the potential well is steep, resulting in a broad overall absorption band. The cross section along the low-frequency coordinate Q_2 with $Q_1 = 0$ leads to a shallow potential, and the overall absorption band becomes narrow. The antiresonance is a consequence of the mixing between the ^2E and $^4T_2$ states represented by the adiabatic potentials. Due to this mixing each point on the two-dimensional adiabatic surfaces has its own distinct relative contributions from the $^4T_2$ and ^2E states. A quantitatively equivalent variation cannot be obtained for the one-dimensional potentials in Figure 4, where the curves along Q_1 do not contain the variation of the $^4T_2$ and ^2E contributions along Q_2 and vice versa. The mixing of the ^2E and $^4T_2$ states leads therefore to a coupling of the two normal coordinates,[30,31] resulting in the nonelliptic contour lines in Figure 5. The two-dimensional surfaces combine the effects of the low- and high-frequency modes with the electronic mixing for each point of the surfaces. This analysis of the two-dimensional surfaces illustrates the specific requirements needed to observe a clear interference dip as shown in Figure 2. Excited state energies for the title compound depend strongly on the exact molecular structure in Figure 1. An exactly octahedral, mononuclear complex is not likely to show an interference dip similar to that of the title compound in Figure 2. The model calculations are not restricted to the adiabatic surfaces, and an essential factor leading to interference dips is the wave packet amplitude transfer between the two surfaces.

We assume the transition to the $^4T_2$ state, defined by the diabatic potential in eq 2, to be fully allowed, and the transition to the ^2E state with the diabatic potential defined by eq 1 to be fully forbidden. The propagation method used here keeps track of amplitude transfer between the surfaces, a very important factor leading to the calculated interference dips in Figure 6. This aspect of our model is best illustrated by the absolute values of the autocorrelation functions $\langle\phi|\phi(t)\rangle$ shown in Figure 7. The autocorrelation for all models drops rapidly from its initial value of 1. The steep decrease observed for the high-frequency one-dimensional model and for the two-dimensional model leads to the broad overall band. In contrast, the decrease along the single coordinate in the one-dimensional model based on the 90 cm^{-1} mode is much slower, leading to an overall bandwidth that is smaller than observed in the experiment. These differences of the initial decrease of $|\langle\phi|\phi(t)\rangle|$ are illustrated in Figure 7. There is a recurrence (maximum) for all models at times shorter than 40 fs. This maximum corresponds approximately to the energy difference between the absorption maxima on both sides of the interference dip in the calculated spectrum. It is a crucial feature always present when interference dips are calculated and arises from the transfer of time-dependent wave function amplitude to the doublet state and back to the quartet state at very short times. The shape of this recurrence has an important influence on the shape of the calculated dip. For the one-dimensional model involving the 90 cm^{-1} mode, the recurrence in Figure 7 occurs as a shoulder on the main decrease. This behavior is due to the shallow potentials and slow wave packet motion, and it leads to a low intensity for the peak on the high-energy side of the interference dip in Figure 6a, one of the major shortcomings of this calculated spectrum in comparison with the experiment. This important discrepancy is intrinsic to all single-coordinate models based on a low-frequency mode, as the decrease of the autocorrelation will always be slow and the recurrence will occur at relatively long times, corresponding to a low energy difference between the origin of the calculated $^4T_2$ band and the maximum following the calculated interference dip. In order to keep the energy of the calculated interference dip close to the experiment, the potential curve for the ^2E state in Figure 4a has to be placed higher in energy by 1200 cm^{-1} than for the one-dimensional model based on the 415 cm^{-1} mode in Figure 4b.

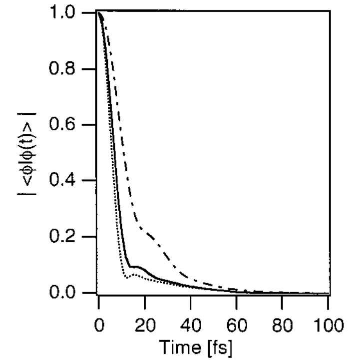

Figure 7. Absolute values of the autocorrelation functions $\langle\phi|\phi(t)\rangle$ used to calculate the spectra in Figure 6. Solid line: two-mode model (415 and 90 cm^{-1}, Figure 6c). Dotted line: one-mode model (415 cm^{-1}, Figure 6b). Dash-dotted line: one-mode model (90 cm^{-1}, Figure 6a).

In the two-dimensional model, the initial decrease of $|\langle\phi|\phi(t)\rangle|$ on the lower adiabatic surface occurs mainly along the steepest gradient of the potential, corresponding to the high-frequency coordinate Q_1. The comparison of the initial decrease of the autocorrelations in Figure 7 shows that this aspect of the two-dimensional model is very similar to the one-dimensional model based on the high-frequency mode in Figure 4b. The steep initial decrease of the autocorrelation function in Figure 7 leads to a calculated intensity distribution around the interference dip in good agreement with the experimental spectrum, as illustrated in Figure 6c. The offset of the minimum of the lower adiabatic potential along the coordinate defining the 90 cm^{-1} mode does not play an important role, but it is important for the upper adiabatic surface, shown in the middle panel of Figure 5. The minimum of the higher energy adiabatic potential surface for the two-dimensional model has a significant offset along the low-frequency coordinate Q_2, but its minimum along Q_1 is very close to the origin of the (Q_1,Q_2) coordinate system, defining the starting region of the time-dependent wave function at $t = 0$. The wave packet amplitude on the upper adiabatic surface moves therefore mainly along the low-frequency coordinate. In order to keep the calculated interference dip at the observed energy, the potential for the ^2E state has to be placed at an energy similar to the one-dimensional model in Figure 4a, where only the offset along the low-frequency coordinate Q_2 is nonzero. The ^2E potential for the two-dimensional model is higher in energy by 950 cm^{-1} than in the one-dimensional model, as summarized in Table 3. The short-time wave packet dynamics on the upper adiabatic surface is therefore determined by the low-frequency mode, underlining

---

(30) Wexler, D.; Zink, J. I. *J. Phys. Chem.* **1993**, *97*, 4903.

(31) Tannor, D. J. *J. Phys. Chem.* **1988**, *92*, 3341.

that the low frequency is essential. A calculated spectrum using two-dimensional potential surfaces along the 317 and 415 cm^{-1} modes does not reproduce the shape of the interference dip well.

The qualitative comparison based on the adiabatic potentials reveals the influence of both coordinates on the calculated spectrum and illustrates that no one-dimensional model is sufficient to analyze the interference dip in the spectra shown in Figure 2. The two-mode model allows us to obtain a good agreement between experimental and calculated spectra for both the intensity distribution and energies of the maxima at the low- and high-energy sides of the interference dip.

Conclusion

Antiresonances in the absorption spectra of $(Et_4N)_3Cr_2F_9$ can be rationalized with a model based on molecular electronic states interacting via spin−orbit coupling. Our analysis shows that at least two molecular modes with frequencies obtained from Raman and absorption spectra define the shape of the interference dip. To our knowledge, this is the first experimental spectrum with an interference dip that clearly involves several modes with different frequencies.

Acknowledgment. We thank Véronique Tessier and Professor Matthias Ernzerhof (Université de Montréal) for carrying out the Gaussian calculation and for helpful discussions. This work was financially supported by the Swiss National Science Foundation and the Natural Sciences and Engineering Research Council (Canada). C.R. thanks the Hans Sigrist foundation for sabbatical support.

Supporting Information Available: Graphical illustrations of the calculated modes listed in Table 2 and the full output of the density functional calculation on $Cr_2F_9^{3-}$. This material is available free of charge via the Internet at http://pubs.acs.org.

IC001364V